Contents list available at CBIORE journal website

International Journal of Renewable Energy Development

Journal homepage: https://ijred.cbiore.id

Research Article

Robust control strategy for optimized IM-4S-VSI-based wind turbine simulator: Assessment for theoretical study

Mouna Zerzeri*, Intissar Moussa, Adel Khedher

University of Sousse, Ecole Nationale d'Ingénieurs de Sousse, LATIS- Laboratory of Advanced Technology and Intelligent Systems, 4002, Sousse, Tunisia

Abstract. Wind turbine emulation faces significant challenges in achieving high dynamic performance while maintaining low-cost and sensorless control architectures suitable for laboratory validation. This paper proposes a software-based wind turbine simulator replicating the dynamic behavior of a 3 kW wind turbine under realistic wind conditions, including quasi-stationary, stochastic, and localized gust (Mexican Hat) profiles. The emulator is implemented using a three-phase induction motor driven by a four-switch voltage source inverter (4S-VSI), controlled via rotor field-oriented control and space vector modulation. A sliding-mode observer (SMO) is employed to estimate rotor speed and flux from stator current measurements, eliminating mechanical sensors. Additionally, an adaptive parameter estimator based on the reactive power method is incorporated into the control loop to identify the rotor resistance in real time. Under nominal loaded operation, the proposed scheme achieves speed tracking errors below 1%, torque errors below 6%, and rotor flux errors below 2% across all wind profiles. When a severe +100% rotor resistance variation is introduced, speed deviation reaches 10% and torque error approaches 20% prior to adaptation, while estimated quantities remain stable, demonstrating observer robustness. Once the reactive power–based adaptation is activated, speed error returns to nearly zero, torque error falls below 5%, stator current error remains under 3%, and flux deviation becomes negligible. The maximum observed speed overshoot under gust excitation is 13.27%, with a settling time of 0.31 s. A quantitative comparison with a conventional six-switch VSI shows that the proposed 4S-VSI reduces switching activity by approximately 43% (from 44.89 kHz to 25.72 kHz equivalent switching frequency), leading to lower switching losses and reduced hardware complexity without compromising dynamic performance. These results demonstrate that the proposed architecture achieves robust observer convergence, accurate wind profile emulation, and significant converter loss reduction, providing a cost-effective and computationally efficient platform for real-time validation of wind energy conversion systems.

Keywords: Wind turbine emulator, Induction motor, 4S-VSI, Sliding mode observer, sensorless control, Reactive power estimation, Parameter adaptation

Received: 2nd Oct 2025; Revised: 5th Feb 2026; Accepted: 26th Feb 2026; Available online: 3rd March 2026

1. Introduction

In response to the rising global electricity demand, the growing costs of fossil fuels, and the imperative to address environmental concerns associated with the high carbon footprint that contributes to global warming and climate change, significant advancements have been made in renewable energy technologies, particularly wind energy. Despite aftershocks from the pandemic and the rise in global commodity prices, wind power has continued to grow (IRENA 2024; IEA 2024), with global installed capacity reaching 1174 GW in 2024, accounting for over 10% of global electricity demand (WWEA 2024a). However, the annual growth rate declined to 11.5%, down from 13.0% in 2023 (WWEA 2024b). This highlights the ongoing need to enhance the efficiency, reliability, and cost-effectiveness of Wind Energy Conversion Systems (WECS) (Farag *et al.* 2017; Hassan *et al.* 2011). Since, various components including mechanical structure, power electronics circuits, and generator and many factors such as turbine size, blades length, and wind velocity affect how much power can be generated, it has been necessary to scale up a Wind Energy Conversion System (WECS) for laboratory tests in order to evaluate new design, to investigate its characteristic performance under different wind velocities, pitch angle, tip-speed ratio, control algorithm, generator load and then to standardize it on the market as training tools for academic or industrial purpose. Nevertheless, large-scale wind turbine installation and maintenance depend on several factors such as space, cost and environmental variations, and time consumption. Consequently, Wind Turbine Simulator (WTS), as cost-effective alternative, is developed and scaled down to laboratory levels in order to perform research, analysis, implementation, and test validation. These simulators replicate both steady-state and dynamic behaviors of real turbines in controlled environments, enabling the development, testing, and validation of new designs and control algorithms without reliance on actual wind resources (Hemeida *et al.* 2013; De Oliveira and Andreoli 2021). WTS are also widely used for educational purposes, performance analysis, and grid integration studies, thus playing a critical role in accelerating wind energy innovation and deployment. Any WTS are designed to replicate the three primary operational regions of wind turbines, namely pitch angle control, maximum power point tracking (MPPT), and parking, using simulation and real-time testing modes (Allouche *et al.* 2019; Kathiresan *et al.* 2020; Farag 2023; Morfin Onofre *et al.* 2021; Sebestyén 2021).

* Corresponding author
Email: mounazer@hotmail.fr (M. Zerzeri)

https://doi.org/10.61435/ijred.2026.61842
ISSN: 2252-4940/© 2026.The Author(s). Published by CBIORE

Typically, these systems consist of two subsystems: a prime mover, often a DC or AC motor emulating the turbine's mechanical behavior, and an electrical subsystem implementing control strategies that mimic wind generator dynamics.

DC motors, particularly separately excited (SEDCM) and permanent magnet variants (PMDCM), are commonly used due to their favorable control characteristics and dynamic response (Benaaouinate *et al.* 2017; Boutabba *et al.* 2025; Kouadria *et al.* 2013; Moussa *et al.* 2022c). Control methods based on DSP, dSPACE, and FPGA platforms have enabled real-time implementation of turbine emulation, including open-loop and PI-controlled systems (Merabet *et al.* 2014; Chinchilla *et al.* 2004; Battaiotto *et al.* 1996; Moussa *et al.* 2019; Moussa *et al.* 2022a; Moussa *et al.* 2022b; Satish Kumar *et al.* 2022). However, because electric motors do not naturally exhibit the inertia of real turbines, inertia compensation is essential for dynamic accuracy (Khan *et al.* 2024; Jing *et al.* 2023). Alternating current machines (ACMs), especially Permanent Magnet Synchronous Motors (PMSMs), have gained attention for their high torque density and responsiveness, with recent studies exploring their use in both open-loop and closed-loop vector control schemes (Yan *et al.* 2016; Chen *et al.* 2017; Nair and Narayanan 2020). Induction Motors (IMs)-based wind turbine emulators are widely adopted due to their robustness, cost-effectiveness, and ability to accurately reproduce the mechanical characteristics of real wind turbines. (Jnayah *et al.* 2023; Kojabadi and Chang 2004; Lu *et al.* 2012; Zerzeri *et al.* 2024a; Zerzeri *et al.* 2024b). However, achieving high-fidelity emulation while maintaining low-cost and sensorless architecture remains a challenging task, particularly when advanced control strategies are required.

In recent years, sensorless control techniques for IM drives have been extensively investigated to eliminate mechanical speed sensors, reduce system cost, and improve reliability (Kumar *et al.* 2015; Mohan *et al.* 2020; Verma *et al.* 2013; Wang *et al.* 2023). Model-based observers such as MRAS (Korzonek et *al.* 2019; Kumar *et al.* 2015; Tu *et al.* 2023), extended Kalman filters (Hassan et al. 2025; Moaveni et al. 2023; Yildiz *et al.* 2024), and sliding mode observers (SMOs) (Che *et al.* 2023; Zaky *et al.* 2018) have been successfully applied in various industrial drive applications. Among these approaches, SMO-based schemes are especially attractive due to their strong robustness against disturbances and parameter uncertainties (Benchaib *et al.* 2002; Li *et al.* 2005; Yang *et al.* 2022; Zerzeri *et al.* 2024a; Zerzeri *et al.* 2024b). Nevertheless, their performance can be significantly degraded by machine parameter variations, particularly rotor resistance mismatches, which directly affect speed and flux estimation accuracy in wide operating ranges.

Several online parameter adaptation techniques have been proposed to address this issue, including rotor time constant identification and stator resistance estimation based on MRAS or signal injection methods (Bednarz *et al.* 2019; Chen *et al.* 2017; Zhao *et al* 2025). While effective, many of these approaches require additional excitation signals, complex tuning procedures, or rely on flux variations that may not always be present during steady-state operation. Moreover, most existing works focus on rotating IM drives and do not explicitly address the specific requirements of wind turbine emulation systems, where smooth torque reproduction, wide-speed operation, and stable behavior under varying wind profiles are critical. While effective, many of these approaches require additional excitation signals, complex tuning procedures, or rely on flux variations that may not always be present during steady-state operation. Moreover, most existing works focus on rotating IM drives and do not explicitly address the specific requirements of wind turbine emulation systems, where smooth torque reproduction, wide-speed operation, and stable behavior under varying wind profiles are critical.

From the power electronics perspective, conventional two-level voltage source inverters (VSIs) are commonly used in wind turbine emulators (Kumar *et al.* 2024; Maheshwari et al. 2023; Rajendran *et al.* 2023). However, these topologies suffer from increased switching losses and higher semiconductor count. The four-switch voltage source inverter (4S-VSI) has recently emerged as a promising alternative, offering reduced cost, lower switching losses, and a compact structure. Despite these advantages, the integration of 4S-VSI topologies with advanced sensorless control and online parameter adaptation strategies for wind turbine emulation remains insufficiently explored in the literature.

In this context, this work proposes a structurally optimized wind turbine simulator based on a three-phase induction motor driven by a four-switch voltage source inverter (4S-VSI), designed to behave as a real turbine within a software environment for theoretical analysis. The simulator is controlled with a rotor flux-oriented vector control strategy, with reference voltages modulated through a modified space vector modulation (SVM) scheme. This design significantly reduces hardware requirements while maintaining high-accuracy voltage synthesis. To enhance observability and robustness, a sliding mode observer (SMO) is incorporated to estimate the rotor speed and flux from stator current measurements, thereby eliminating the need for costly mechanical sensors. Moreover, an adaptive online estimator based on the reactive power method is added to identify the rotor resistance in real-time, thus ensuring control stability under parameter variations such as thermal drift or aging effects. Unlike conventional MRAS- or signal-injection-based approaches, the proposed reactive power adaptation law enables online rotor resistance estimation without requiring additional excitation signals or flux variations, making it particularly suitable for steady-state and low-dynamic operating conditions typical of wind turbine emulation. The simulator is tested under multiple wind scenarios, including linear-constant, sinusoidal, and Mexican hat profiles, and validated via comprehensive real-time simulations of a 3 kW turbine (Moussa et al. 2022c).

2. WTS modeling

A simulator for wind turbine is a computer-based system or software application designed to replicate the behavior and performance of real wind turbines in a virtual environment. It employs mathematical models and algorithms to mimic the WT dynamics and characteristics, allowing users to analyze and study their operation without the need for physical prototypes or real-world installations. It provides accurate various aspects representations of wind turbines, such as aerodynamics, mechanical components, electrical systems, and control algorithms (Donnou *et al.* 2020; Salami *et al.* 2022). The wind turbine simulator's typical arrangement is depicted in Fig. 1. In the present section, the mathematical modeling of wind turbine, inverter, and induction motors is developed.

2.1 Aerodynamic model

Aerodynamic model plays a crucial role in depicting the energy conversion process, where the air mass motion at a specific velocity is transformed into rotational motion within the turbine (Donnou *et al.* 2020; Guenoukpati *et al.* 2020). This rotational motion, in turn, is used to generate mechanical energy transmitted to the generator shaft. The energy harnessed from the wind essentially stems from the kinetic energy possessed by

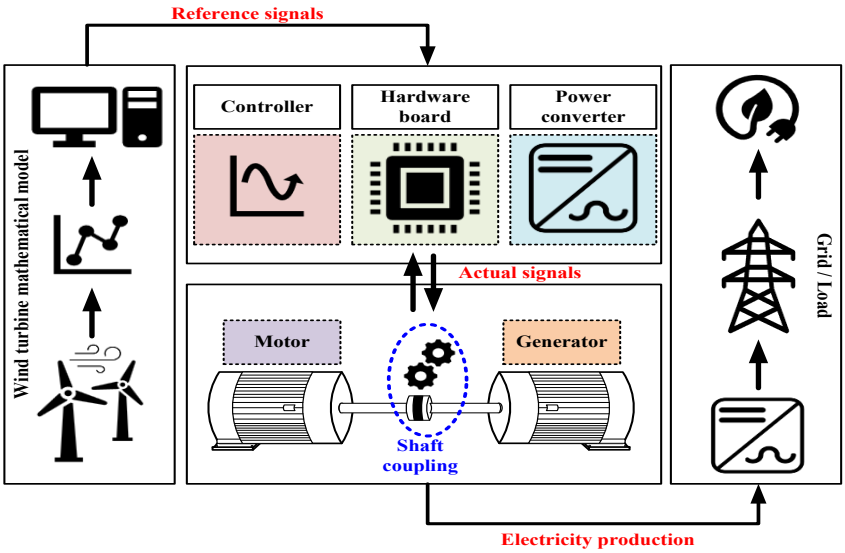

Fig. 1 WTS general configuration

substantial air masses in motion across the Earth's surface. In this study, we considered three wind shapes as linear/constant (Eq. (1)), stochastic (Eq. (2)) and Mexican hat (Eq. (3)) expressed as follows:

$$W_s(t)=\begin{cases} 4.2 \quad if \quad t<1s \\ 1.12t-1.4 \quad if \quad 1s<t<2s \\ 9.8 \quad if \quad 2s<t<2.5s \\ -0.32t+16.2 \quad if \quad 2.5s<t<3.5s \\ 8.2 \quad if \quad t>3.5s \end{cases} \tag{1}$$

$$W_s(t)=\bar{W}+\sum_{i=1}^{7} k_i \sin(a_i \omega_w t) \tag{2}$$

$$W_s(t)=\bar{W}+\left(W_s^g-\bar{W}\right)\left(1-\frac{(t-t_0)^2}{\delta^2}\right)e^{-\frac{(t-t_0)^2}{2\delta^2}} \tag{3}$$

Where W_s is the wind speed, $\bar{W}$ is the average speed, W_s^g is the maximum speed, k_i, a_i, and ω_w are constants whose coefficients are defined in the Appendix A Table A1, t_0 is the gust center time, whereas δ represents its shape factor.

Since the powertrain rigidity is uncertain, the turbine's friction coefficient and momentum need to be combined with those of the generator to ensure proper functioning. As the turbine rotor blades receive wind kinetic energy, it is converted into mechanical power. The aerodynamic power conversion of the wind turbine is expressed as (Maeda *et al.* 2017; Moussa *et al.* 2022c):

$$P_t=\frac{\rho A W_s^3 C_p(\lambda,\beta)}{2} \tag{4}$$

Where P_t is the turbine mechanical power, ρ is the air density, A is the area swept by the turbine blades, $C_p(\lambda,\beta)$ is the power coefficient, defined as a function of the tip-speed ratio λ and pitch angle β.

The analytical formulation of the power coefficient, as well as the corresponding turbine torque expression, are extensively developed in our previous work (Moussa *et al.* 2022c).

2.2 Mechanical model

The mechanical model consists of a two-mass system interconnected by shafts, where the system's shaft speed and torque directly reflect the available mechanical power. In a real turbine system, when coupling the prime mover to the generator, an accelerating torque is introduced to drive the combined turbine-generator subsystem. This torque represents the difference between the turbine and generator torques, which is fundamental to understanding the dynamic interaction between the two components. In the real wind turbine generator system (WTGS), the mechanical dynamics can be expressed in the Laplace domain by the following transfer function:

$$\frac{\Omega_t(s)}{\Delta T_{t-g}(s)}=\frac{1}{J_{t-g}s+f_{t-g}} \tag{5}$$

where J_{t-g} represents the equivalent inertia of the turbine–generator set and f_{t-g} is the combined viscous friction coefficient.

In the emulator, a three-phase IM replaces the turbine–generator mechanical subsystem, as shown in Fig. 2. Since the motor inertia differs from the actual turbine inertia, a torque compensation mechanism is introduced to ensure dynamic equivalence between the real system and its emulator. The resulting mechanical transfer function of the motor–generator subsystem used for emulation is therefore given by:

$$\frac{\Omega_{emu}(s)}{\Delta T_{m-g}(s)}=\frac{1}{J_{m-g}s+f_{m-g}} \tag{6}$$

Where J_{m-g} and f_{m-g} are the combined inertia and viscous friction of the motor–generator emulator system.
The detailed derivation of the inertia compensation mechanism and intermediate dynamic equations are provided in Appendix C.

2.3 Electrical model

For this study, the electrical model is allocated to the four-switch voltage source inverter used for induction motor drive.

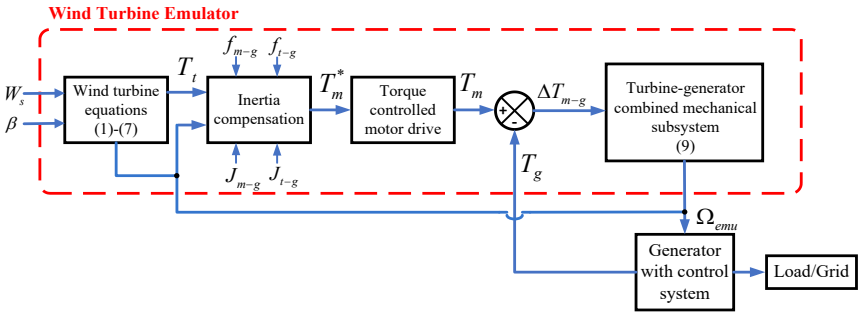

Fig. 2 WTS model with inertia emulation

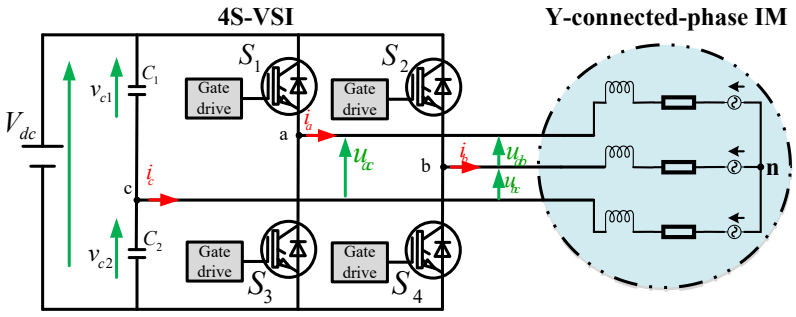

Fig. 3 4S-VSI for IM drive

Unlike traditional inverters that use six switches, the 4S-VSI as a low-cost attractive power topology utilizes only four switches, making it an efficient solution for various applications. By varying the switching events timing and duration, the output voltage across the load can be adjusted to generate the desired AC waveform making the IM speed react as wind speed velocity at laboratory. In the conventional topology for the 4S-VSI and induction motor association as shown in Fig. 3, the midpoint of the DC-link capacitors is connected to the IM terminal phase through Y-connected coupling.

By appropriately controlling the switching states, the inverter generates the required line voltages to emulate wind-speed-induced motor dynamics in laboratory conditions. The line-to-line output voltages u_{ac}, u_{bc}, u_{ab} of the 4S-VSI can be expressed as a function of the DC-link voltage and switching functions as:

$$\begin{cases} u_{ac} = \dfrac{V_{DC}}{2}\left(2s_1 - v_{c1}\right) \\ u_{bc} = \dfrac{V_{DC}}{2}\left(2s_2 - v_{c2}\right) \\ u_{ab} = \dfrac{V_{DC}}{2}\left(2s_1 - 1\right) - \dfrac{V_{DC}}{2}\left(2s_2 - 1\right) \end{cases} \tag{7}$$

The inverter operates under the SVM strategy, which ensures balanced voltage synthesis and optimal utilization of the DC-link voltage. The reference phase voltages are generated through PWM modulation based on the rotor electrical position and control objectives. The detailed derivation of the voltage relationships and DC-link decomposition is provided in Appendix D.

3. Mathematical development of the WTS controller

3.1 WTS controller design

The WTS is controlled by a robust sliding-mode observer-based rotor flux-oriented vector control (FOC) strategy combined with an online adaptation mechanism of rotor resistance using the reactive energy method. The block diagram of the overall WTS controller design is described in Fig. 4.

The emulator receives its reference rotor speed from a comprehensive wind turbine model that incorporates physical and aerodynamic parameters, including wind speed dynamics, the power coefficient curve, turbine topology, mechanical characteristics, and the gear ratio of the drivetrain. This reference model ensures that the emulator reflects the authentic response of a real turbine under varying wind scenarios. The control system is composed of three subsystems. First, a sliding mode observer is employed to estimate both rotor flux and mechanical speed from stator current measurements, thereby enabling a fully sensorless operation. To enhance robustness, the SMO is improved by an online adaptive mechanism that continuously estimates the rotor time constant, compensating for thermal and parametric variations. Second, the estimated flux and speed are fed into a rotor FOC algorithm that computes the stator voltage references required to reproduce the reference torque generated by the turbine model. Third, an advanced space vector pulse width modulation block for a *4S-VSI* topology synthesizes the desired voltage vectors. This reduced-switch modulation strategy minimizes hardware complexity while preserving high control resolution and generates the gate signals for the inverter switches. The inverter output drives a three-phase induction motor, which acts as the prime mover to emulate the mechanical dynamics of a wind turbine.

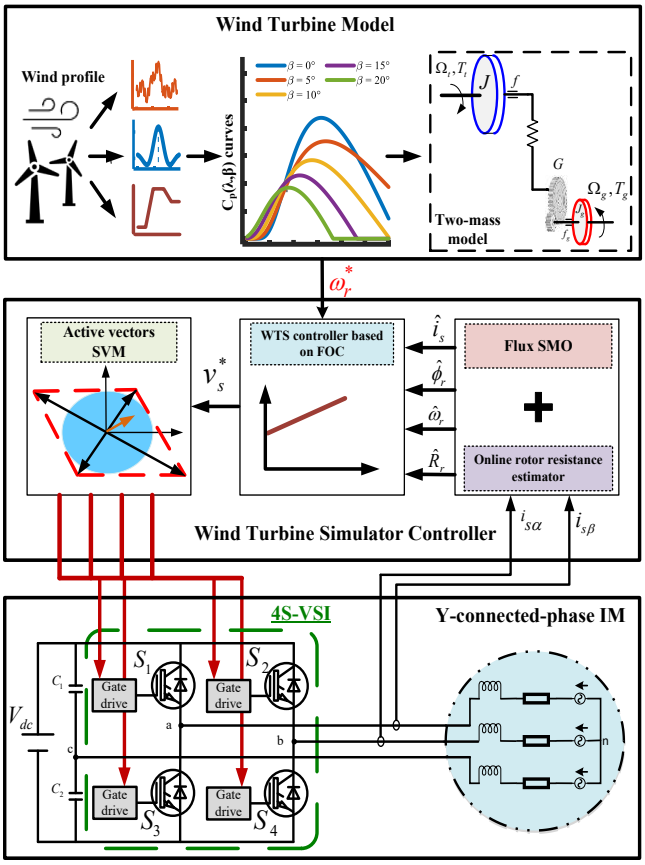

Fig. 4 General control scheme of the proposed wind turbine simulator.

3.2 IM dynamic and state models

This section focuses on the mathematical modeling of the IM controller in the complex form in order to establish an appropriate proof guide to apply suitable control laws for its operation as a wind turbine simulator in a software platform. The induction machine is modeled in the stationary complex reference frame. Under standard assumptions of sinusoidal windings and linear magnetic behavior, the IM dynamic equations can be expressed in terms of the stator current vector and rotor flux vector as follows:

$$\begin{cases} \dfrac{d\vec{I}_s}{dt} = -\left[\dfrac{\left(R_s + \left(\dfrac{M}{L_r}\right)^2 R_r\right)}{\sigma L_s} + j\omega_s\right]\vec{I}_s - \dfrac{M}{\sigma L_s L_r}\left(-\dfrac{R_r}{L_r} + j\omega\right)\vec{\phi}_r + \dfrac{1}{\sigma L_s}\vec{V}_s \\ \dfrac{d\vec{\phi}_r}{dt} = \dfrac{MR_r}{L_r}\vec{I}_s - \left[\dfrac{R_r}{L_r} + j(\omega_s - \omega)\right]\vec{\phi}_r \end{cases} \quad (8)$$

where $\vec{I}_s$ denotes the stator current vector, $\vec{\phi}_r$the rotor flux vector, ω the rotor electrical speed, and $\vec{V}_s$ the stator voltage vector. $\sigma = 1 - \frac{M^2}{L_s L_r}$ is the dispersion coefficient

The electromagnetic torque produced by the machine is given in complex form by:

$$T_{em} = \frac{3}{2} n_p \frac{M}{L_r} \Im m\left(\vec{I}_s . \vec{\phi}^*_r\right) \quad (9)$$

This formulation highlights the coupling between stator current and rotor flux, which is exploited in the control strategy. Based on the above relations, the IM control-oriented model can be written in a compact state-space form by selecting the stator current and rotor flux vectors as state variables:

$$\dot{\vec{X}} = [\bar{A}]\vec{X} + [\bar{B}]\vec{U} \quad (10)$$

with $\vec{X} = \left[\vec{I}_s \quad \vec{\phi}_r\right]^T$ is the state vector and $\vec{U} = [\vec{V}_s]$ is the control vector. $[\bar{A}]$ and $[\bar{B}]$ are, respectively, the state and control matrices defined in the complex form as follows:

$$[\bar{A}] = \begin{bmatrix} -\left[\dfrac{\left(R_s + \left(\dfrac{M}{L_r}\right)^2 R_r\right)}{\sigma L_s} + j\omega_s\right] & -\dfrac{M}{\sigma L_s L_r}\left(-\dfrac{R_r}{L_r} + j\omega\right) \\ \dfrac{M}{\tau_r} & -\dfrac{1}{\tau_r} + j(\omega_s - \omega) \end{bmatrix}$$

$$[\bar{B}] = \begin{bmatrix} \dfrac{1}{\sigma L_s} \\ 0 \end{bmatrix}$$

3.3 Sliding-mode observer formulation

In this section, we develop a rotor flux observer for IM based on the sliding-mode technique. According to the state equation (10), the state observer basic structure is expressed as:

$$\begin{bmatrix}\dot{\vec{I}}_s\\ \dot{\vec{\phi}}_r\end{bmatrix}= \begin{bmatrix}-\frac{\left[\left(R_s+\left(\frac{M}{L_r}\right)^2 R_{re}\right)\right]}{\sigma L_s}+j\omega_s & -\frac{M}{\sigma L_s L_r}\left(\frac{-R_{re}}{L_r}+j\omega\right)\\ \frac{M}{L_r}R_{re} & -\left[\frac{R_{re}}{L_r}+j(\omega_s-\omega)\right]\end{bmatrix}\begin{bmatrix}\vec{I}_s\\ \vec{\phi}_r\end{bmatrix}+ \begin{bmatrix}\frac{1}{\sigma L_s}\\ 0\end{bmatrix}[\vec{V}_s]+\begin{bmatrix}A_{11}+jA_{21}\\ A_{31}+jA_{41}\end{bmatrix}sign\left(\Re e(\vec{S})\right)+ \begin{bmatrix}A_{12}+jA_{22}\\ A_{32}+jA_{42}\end{bmatrix}sign\left(\Im m(\vec{S})\right) \quad (11)$$

The estimated current and flux vectors are denoted respectively by $\vec{I}_s$ and $\vec{\phi}_r$. $[\bar{A}_I]=\begin{bmatrix}A_{11}+jA_{21}\\ A_{31}+jA_{41}\end{bmatrix}^T$, $[\bar{A}_\phi]=\begin{bmatrix}A_{31}+jA_{41}\\ A_{32}+jA_{42}\end{bmatrix}^T$ are the current and flux gain matrices respectively. $\vec{S}_I=S_1+jS_2$is the sliding surface vector. *sign(.)* is the sign function. R_{re} is the estimated rotor resistance. Let's define by $\vec{E}_I=\vec{I}_s-\hat{\vec{I}}_s$ and $\vec{E}_\phi=\vec{\phi}_r-\hat{\vec{\phi}}_r$ the observation errors for current and flux.

3.3.1. Mathematical development without parametric variation case

In the case where the WTS operates without parameter variations, the equation describing the observation errors is given by:

$$\begin{bmatrix}\dot{\vec{E}}_I\\ \dot{\vec{E}}_\phi\end{bmatrix}= \begin{bmatrix}-\frac{\left[\left(R_s+\left(\frac{M}{L_r}\right)^2 R_r\right)+j\omega_s\right]}{\sigma L_s} & -\frac{M}{\sigma L_s L_r}\left(\frac{-R_r}{L_r}+j\omega\right)\\ \frac{M}{L_r}R_r & -\left[\frac{R_r}{L_r}+j(\omega_s-\omega)\right]\end{bmatrix}\begin{bmatrix}\vec{E}_I\\ \vec{E}_\phi\end{bmatrix} -\begin{bmatrix}A_{11}+jA_{21}\\ A_{31}+jA_{41}\end{bmatrix}sign\left(\Re e(\vec{S})\right)-\begin{bmatrix}A_{12}+jA_{22}\\ A_{32}+jA_{42}\end{bmatrix}sign\left(\Im m(\vec{S})\right) \quad (12)$$

Since stator currents can be measured directly from the test bench via digital acquisition, observation of these quantities enables us to monitor the dynamic and accuracy of non-measurable quantities such as rotor flux. The selected sliding surface is directly related to the stator current error by the following relation:

$$\vec{S}=\left(\frac{kR_r}{L_r}-jk\omega\right)^{-1}\vec{E}_I \quad (13)$$

Where $k=\frac{M}{\sigma L_s L_r}$. Thus, the current gain matrix is chosen as follows:

$$[\bar{A}_I]=\begin{bmatrix}A_{11}+jA_{21}\\ A_{12}+jA_{22}\end{bmatrix}^T=\left(\frac{kR_r}{L_r}-jk\omega\right)[\delta_1 \quad \delta_2] \quad (14)$$

Where δ_1 and δ_2 are two positive constants subsequently determined by the Lyapunov stability analysis in the nominal case (without parameter variation) and in the presence of parameter variations, respectively. In order to calculate the flux adjustment gain, we consider it converging to the sliding surface $S=0$. To do this, we determine the flux errors dynamic behavior in sliding mode. The cancellation of S and $\dot{S}$ results in the current error cancellation and its derivative. Therefore, the flux errors can be expressed as follows:

$$\dot{\vec{E}}_\phi=\left[\left(-\frac{R_r}{L_r}+j(\omega_s-\omega)\right)-[A_{31}+jA_{41} \quad A_{32}+jA_{42}] \times[A_{11}+jA_{21} \quad A_{12}+jA_{22}]^{-1}\left(\frac{kR_r}{L_r}-jk\omega\right)\right]\vec{E}_\phi \quad (15)$$

Given that the observer dynamics are based on the exponential convergence of the flux error; we can impose that $\dot{\vec{E}}=-Q\vec{E}_\phi$. Where Q is a positive constant. Hence, the flux gain matrix can be computed as follows:

$$\bar{A}_\phi= \begin{bmatrix}\left(-\frac{R_r}{L_r}+j(\omega_s-\omega)+Q\right)\delta_1 & \left(-\frac{R_r}{L_r}+j(\omega_s-\omega)+Q\right)\delta_2\end{bmatrix} \quad (16)$$

It should be noted that the sliding-mode observation system stability is closely linked to its convergence to the sliding surface. This stability depends on the appropriate parameters choice. The Lyapunov function is defined as follows:

$$V=\frac{1}{2}\vec{S}^T\vec{S} \quad (17)$$

To ensure the cancellation of $\vec{S}$, we must check that $\dot{V}<0$. Thus, the stability condition is verified as:

$$\left(\delta_1 sign(S_1)+\delta_2 sign(S_2)\right)\geq\left|\vec{E}_\phi\right| \quad (18)$$

3.3.2. Mathematical development with parametric variation case

Given that the motor rotor resistance is not constant, and with the aim to find a robust control, we propose an equation set, considering the IM rotor constant variation. Let's define $\Delta R_r=R_r-\hat{R}_r$. Subsequently, the error system is rewritten as follows:

$$\begin{bmatrix}\dot{\vec{E}}_I\\ \dot{\vec{E}}_\phi\end{bmatrix}= \begin{bmatrix}-\frac{\left[\left(R_s+\left(\frac{M}{L_r}\right)^2 R_r\right)+j\omega_s\right]}{\sigma L_s} & -k\left(\frac{-R_r}{L_r}+j\omega\right)\\ \frac{M}{L_r}R_r & -\left[\frac{R_r}{L_r}+j(\omega_s-\omega)\right]\end{bmatrix}\begin{bmatrix}\vec{E}_I\\ \vec{E}_\phi\end{bmatrix} +\begin{bmatrix}-\frac{kM}{L_r}\Delta R_r & \frac{k}{L_r}\Delta R_r\\ \frac{M}{L_r}\Delta R_r & -\frac{\Delta R_r}{L_r}\end{bmatrix}\begin{bmatrix}\vec{I}_s\\ \vec{\phi}_r\end{bmatrix}- \begin{bmatrix}A_{11}+jA_{21} & A_{12}+jA_{22}\\ A_{31}+jA_{41} & A_{32}+jA_{42}\end{bmatrix}\begin{bmatrix}sign(S_1)\\ sign(S_2)\end{bmatrix} \quad (19)$$

As before, we define a Lyapunov function to find a stability condition in this case, $\dot{V}<0$:

$$\dot{V}=\vec{S}\left[\vec{E}_\phi+\frac{\Delta R_r}{\left(\frac{k}{L_r}R_r\right)^2+(k\omega)^2}\frac{k}{L_r}\left(\frac{kR_r}{L_r}-jk\omega\right)\left(\vec{\phi}_r-M\vec{I}_s\right)\right.$$

$$-\frac{\Delta}{\left(\frac{k}{L_r}\right)}-\left(\delta_1 sign(S_1)+\delta_2 sign(S_2)\right)\Big] < 0 \quad (20)$$

Let's assume that $\gamma = \frac{k}{L_r}\frac{\Delta R_r}{\left(\frac{k}{L_r}R_r\right)^2+(k\omega)^2}$.

The same approach, as above, is applied to search for the stability conditions keeping the rotor resistance error. In this case, the stability condition for parametric variation is written as follows:

$$\dot{V} < 0 \Leftrightarrow \left(\delta_1 sign(S_1)+\delta_2 sign(S_2)\right) > \left|\vec{E}_\phi + \gamma\left(\frac{kR_r}{L_r} - jk\omega\right)\left(\vec{\phi}_r - M\vec{I}_s\right)\right| \quad (21)$$

3.4 Rotor resistance online adaptation by reactive energy method

To compensate for rotor resistance variations induced by thermal and operating conditions, an online adaptive estimation scheme based on the machine reactive power is adopted. The method relies on the instantaneous energy balance of the induction machine and does not require additional sensors or complex optimization procedures. The complex form of the IM reactive power is defined as the imaginary part of the scalar product between the stator voltage vector and the complex conjugate of the stator current vector. By combining Faraday's law with the stator voltage equations and neglecting the stator resistance, the reactive power can be reformulated as a function of stator currents and rotor flux components. This relationship allows establishing a direct link between the reactive power and the rotor resistance. Based on this formulation, the rotor resistance adaptation law is derived as:

$$\hat{R}_r = \frac{\Im m\left(\vec{V}_s.\vec{I}^*_s\right)+\frac{M}{L_r}\Im m\left[j(\omega_s-\omega)\vec{\phi}_r.\vec{I}^*_s\right]-\sigma L_s \Im m\left[\dot{\vec{I}}_s.\vec{I}^*_s\right]}{\frac{M}{L_r^2}\Im m\left[\left(M\vec{I}_s-\vec{\phi}_r\right).\vec{I}^*_s\right]} \quad (22)$$

where $\hat{R}_r$ denotes the estimated rotor resistance.

4. Simulation results and discussion

This section evaluates the dynamic and robustness performance of the proposed WTS under meteorologically representative wind excitations and significant electrical parameter perturbations. Simulations were conducted in MATLAB/Simulink using the aerodynamic and mechanical parameters of a 3 kW horizontal-axis wind turbine (Appendix A, Table A2) and the induction machine parameters listed in Appendix A, Table A3. The wind excitation profiles were designed to reflect distinct atmospheric phenomena commonly encountered in small-scale wind energy systems operating within the atmospheric boundary layer (ABL). The simulation timeline is segmented into two phases: an unloaded startup phase (0 – 3 s) and a loaded operating phase (3 – 10 s), during which the load torque is made proportional to the rotor speed. The loaded phase is further divided into three cases: (i) baseline operation with a standard Sliding Mode Observer (SMO), (ii) performance under rotor resistance variation introduced at 4.5 s, and (iii) an adaptive observer based on reactive power estimation activated at 5.5 s for fault compensation. A smooth exponential variation of rotor resistance is introduced, reaching up to 100% of its nominal value to emulate thermal and parametric drift effects commonly encountered in induction machine operation. The corresponding mathematical expression is provided in Appendix B (Eq. B.1). Key mechanical and electrical variables such as rotor speed, electromagnetic torque, stator currents, and rotor flux, are analyzed through both qualitative waveforms and quantitative performance indicators.

4.1 Meteorological characterization of wind profiles and dynamic excitation

Three wind profiles are considered (linear/constant, Mexican Hat, and stochastic) as input signals to evaluate the response of the IM operating as WTS under both steady-state and dynamic conditions.

4.1.1 Linear/constant profile

The first wind excitation considered in this study is the linear/constant profile. This later represents quasi-stationary wind conditions typically associated with low-turbulence IEC Class III sites (Larsen *et al.* 2008; International Electrotechnical Commission 2019), where the mean speed predominates and turbulence intensity remains relatively limited. Such conditions are characteristic of stable ABL regimes with weak vertical mixing and minimal short-term wind speed fluctuations. From a control perspective, this profile provides low-frequency excitation and therefore primarily evaluates the steady-state tracking capability of the proposed control scheme rather than its robustness under strong dynamic perturbations. Because the aerodynamic torque varies smoothly under these conditions, the mechanical acceleration of the rotor remains moderate, and the induction machine operates close to electromagnetic equilibrium. As a result, torque ripple is limited, and stator current harmonics remain within moderate bounds, reflecting stable flux–torque decoupling and consistent observer convergence. Fig. 5 illustrates the simulator configuration under the linear/constant wind profile. Specifically, Fig. 5(a) shows the temporal evolution of the imposed wind speed, Fig. 5(b) presents the online rotor resistance adaptation mechanism, and Fig. 5(c) depicts the corresponding load torque variation applied to the induction machine during this operating scenario.

4.1.2 Stochastic profile

The second wind profile adopted in this study was generated using a Monte Carlo–based stochastic approach, allowing the

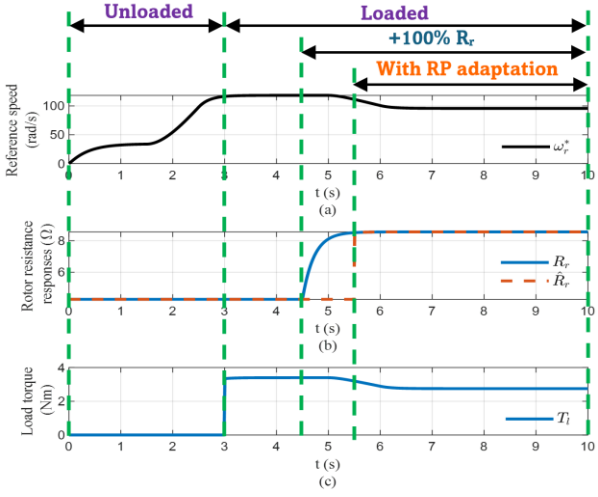

Fig. 5 Simulator configuration for a linear/constant wind profile: (a) Reference speed, (b) Rotor resistance response, (c) Load torque scenarios.

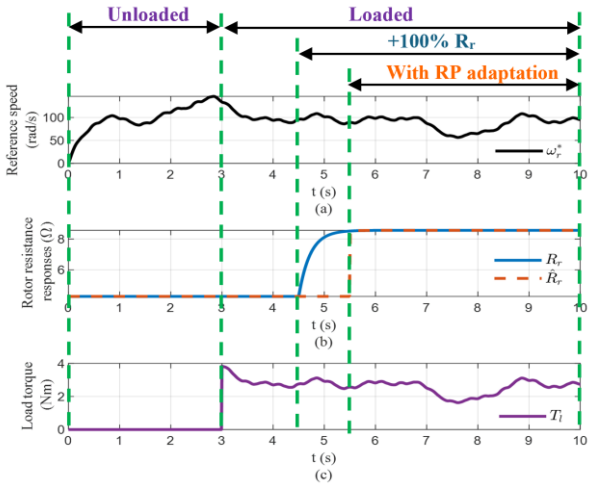

Fig. 6 Simulator configuration for a stochastic wind profile: (a) Reference speed, (b) Rotor resistance response, (c) Load torque scenarios.

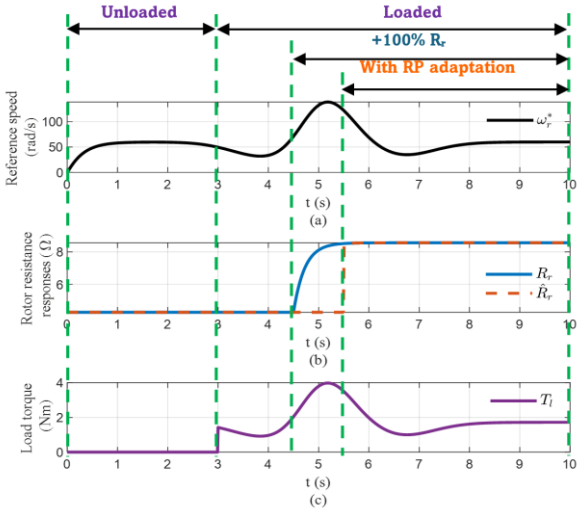

Fig. 7 Simulator configuration for a Mexican hat wind profile: (a) Reference speed, (b) Rotor resistance response, (c) Load torque scenarios.

synthesis of realistic random wind scenarios derived from long-term historical measurements provided by (Météo-France 2019). The statistical characteristics of wind speed, direction, and turbulence intensity were extracted from probabilistic distributions fitted to hourly data recorded at the Brest-Guipavas meteorological station over the 1995–2019 period (Météo-France 2019; Rubinstein *et al.* 2016).

This stochastic profile reproduces turbulent wind conditions typically associated with IEC Class A environments (Larsen *et al.* 2008; International Electrotechnical Commission 2019), where elevated turbulence intensity and rapid fluctuations arise from atmospheric shear instabilities, terrain-induced roughness effects, and boundary-layer mixing processes. Such turbulence-dominated regimes are representative of highly dynamic ABL behavior, particularly in coastal and moderately rough terrains. The resulting simulator configuration is depicted in Fig. 6. As shown in Fig. 6(a), the reference rotor speed generated under this stochastic excitation exhibits irregular, broadband fluctuations, in contrast to the smooth evolution observed under the linear profile. These rapid variations reflect the continuous aerodynamic torque perturbations induced by turbulent wind components. Fig. 6(b) presents the evolution of rotor resistance. The abrupt step introduced at t = 4.5 s emulates a severe thermal drift, which alters the rotor time constant and temporarily disrupts model consistency. Once the reactive power–based adaptation is activated at t = 5.5 s, the estimated rotor resistance converges smoothly toward the imposed value. The convergence is monotonic and free of oscillations, indicating stable parameter identification even under persistent turbulence-induced excitation. This behavior confirms that reactive power remains a reliable indicator of rotor time-constant mismatch, even under broadband stochastic disturbances. Fig. 6(c) shows the load torque proportional to speed. Under stochastic wind conditions, torque fluctuations are continuous and irregular, reflecting turbulent energy packets interacting with the rotor.

4.1.3 Mexican Hat Profile

The third wind profile adopted in this study is the so-called Mexican Hat waveform, which represents a localized gust event modeled by a Ricker wavelet. Unlike stochastic excitation, this profile introduces a structured, time-localized energy packet (Addison 2002; Torrence & Compo 1998). Fig. 7(a) shows the reference speed under gust excitation. The speed rises sharply during the gust peak and then symmetrically decreases. This structured acceleration–deceleration sequence corresponds to coherent atmospheric gust structures observed in convective boundary layers. Fig. 7(b) shows the rotor resistance tracking behavior. The imposed +100% variation at 4.5 s induces model mismatch. However, the adaptation mechanism converges rapidly despite the gust-induced transient energy. The structured nature of the Mexican Hat excitation provides sufficient dynamic richness for accurate parameter identification without introducing persistent broadband noise. As a result, convergence is faster and smoother compared to the stochastic case. Fig. 7(c) illustrates the load torque response during the gust event. The torque follows the speed increase, reaching a peak during maximum gust intensity.

4.2 Dynamic response under nominal and perturbed conditions

The complete electromechanical responses of the proposed wind turbine simulator under the three considered wind excitation profiles are illustrated in Figs. 8–10. Each figure provides a four-dimensional view of system behavior, including rotor speed tracking (a), electromagnetic torque dynamics (b), stator current reconstruction (c), and rotor flux evolution (d).

4.2.1 Controller performance under linear/constant profile

The controller performance under linear wind excitation is evaluated in Fig. 8. This profile introduces predominantly low-frequency aerodynamic excitation and therefore primarily assesses steady-state tracking capability rather than disturbance rejection under strong turbulence (International Electrotechnical Commission 2019). The reference, real, and estimated speeds, as depicted in Fig. 8(a), are almost perfectly superimposed during nominal operation. The absence of oscillatory components confirms that aerodynamic forcing remains smooth and slowly varying. This behavior is consistent with wind energy conversion theory, where mechanical inertia acts as a low-pass filter attenuating high-frequency torque components (Heier 2014). Because the aerodynamic torque evolves gradually, mechanical acceleration remains moderate and no dynamic overshoot appears. The estimated speed

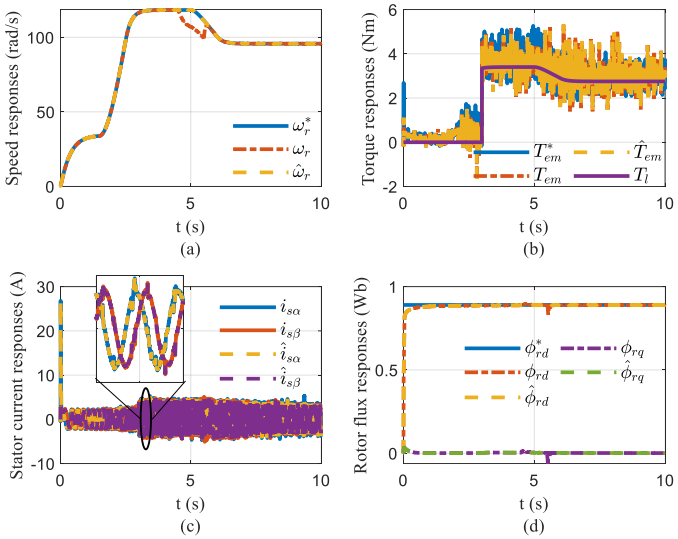

Fig. 6 Dynamic responses of the wind turbine simulator under the linear/constant wind profile: (a) reference, real, and estimated rotor speed; (b) reference, real and estimated electromagnetic torque with load torque; (c) real and estimated stator currents in the α–β reference frame; (d) reference, real, and estimated rotor flux in the d–q reference frame.

converges rapidly during start-up and remains aligned with the real speed, indicating that the SMO successfully enforces the sliding condition under low excitation. At t = 4.5 s, a 100% increase in rotor resistance is introduced. A transient deviation is clearly visible in the real speed, whereas the estimated speed remains practically unaffected. This demonstrates that the observer remains insensitive to rotor time-constant variation, preserving estimation consistency despite severe parametric drift. Once the reactive power–based adaptation is activated at t = 5.5 s, the real speed progressively realigns with the reference trajectory, while the estimated speed remains stable throughout the disturbance. As can be seen in Fig. 8(b), the starting torque exhibits oscillations during the initial transient due to the (i) mismatch between initial machine states and observer estimates and (ii) switching harmonics introduced by the 4S-VSI under SVM. At t = 3 s, a speed-proportional mechanical load is applied, emulating realistic aerodynamic torque behavior. This marks the transition from inertial acceleration to electromechanical equilibrium, where electromagnetic torque balances load torque. The introduction of load increases effective damping and attenuates torque ripple. Under the linear profile, torque remains smooth with minimal steady-state oscillation. When rotor resistance increases at t = 4.5 s, the rotor time constant is altered, temporarily disturbing torque equilibrium. The real torque deviates, while the estimated torque remains stable, confirming that estimation robustness is preserved and that the adaptation acts primarily on the real variables, not the observer. After adaptation, the real torque rapidly converges to its reference with negligible residual error.

The stator currents in the α–β frame, illustrated in Fig. 8(c), retain nearly sinusoidal waveforms throughout the operation, confirming the effectiveness of the 4S-VSI modulation strategy and limited harmonic distortion. During loaded operation, current magnitude increases consistently with torque demand. No distortion or instability appears during rotor resistance variation, indicating stable inverter and current-loop behavior. The real and estimated rotor flux components in the d–q reference frame are given Fig. 8(d). The rotor flux components remain well decoupled, demonstrating proper separation between flux and torque components. Estimated flux aligns closely with real flux during all phases. When rotor resistance is perturbed, the real flux shows slight deviation, whereas the estimated flux remains practically unaffected. After adaptation, the deviation becomes negligible. As a result, under low-frequency excitation, the proposed scheme ensures accurate tracking and strong robustness against parametric variation.

4.2.2 Controller performance under stochastic profile

The controller performance under a stochastic wind profile is assessed in Fig. 9. This profile introduces broadband, irregular excitation representative of IEC Class A turbulence (Larsen et al. 2008). Unlike the linear case, this profile evaluates observer robustness under persistent dynamic excitation. As depicted in Fig. 9(a), the real rotor speed exhibits continuous small-amplitude fluctuations superimposed on the mean trajectory, reflecting turbulence-induced aerodynamic torque variability. Mechanical inertia attenuates but does not eliminate these fluctuations. The estimated speed accurately reproduces both the mean trajectory and the high-frequency components without phase delay or amplification. This indicates that the SMO maintains robustness under bounded disturbances and does not introduce artificial oscillations. When rotor resistance is doubled at t = 4.5 s, the real speed deviates more noticeably than in the linear case due to the interaction between turbulence and altered rotor time constant. However, the estimated speed remains stable, confirming observer insensitivity to parametric uncertainty. After adaptation, the real speed converges smoothly back to reference. Fig. 9(b) shows that the torque exhibits persistent oscillatory modulation due to broadband aerodynamic forcing.

Unlike Fig. 8(b), oscillations are continuous rather than transient. The estimated torque closely matches the real torque amplitude and frequency content, demonstrating sufficient observer bandwidth. During rotor resistance variation, the real torque amplitude increases temporarily due to flux misalignment. The estimated torque remains coherent and does not diverge, confirming that estimation stability is preserved even under combined turbulence and parametric drift. Moreover, the current magnitude fluctuates continuously under the stochastic profile (Fig. 9(c)), reflecting real-time torque adaptation. Despite broadband excitation, current waveforms remain sinusoidal and free of instability. No additional harmonic distortion appears during rotor resistance variation. The real

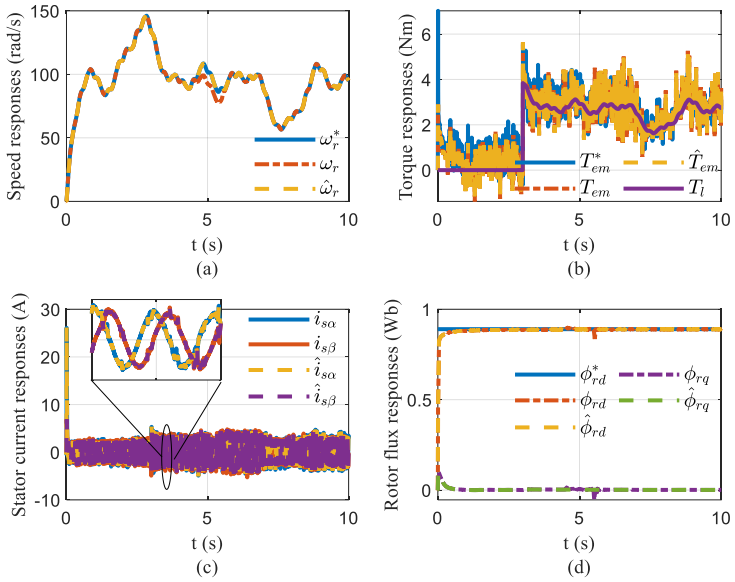

Fig. 9 Dynamic responses of the wind turbine simulator under the stochastic wind profile: (a) reference, real, and estimated rotor speed; (b) reference, real and estimated electromagnetic torque with load torque; (c) real and estimated stator currents in the α–β reference frame; (d) reference, real, and estimated rotor flux in the d–q reference frame.

flux exhibits slight oscillatory modulation caused by turbulence, as shown in Fig. 9(d). However, the estimated flux remains tightly aligned with the real one. Even during parameter variation, flux estimation remains stable (Zerzeri *et al.* 2026;). Once adaptation is activated, real and estimated flux trajectories become practically indistinguishable. Under turbulence-dominated conditions, the observer maintains convergence and disturbance rejection without instability.

4.2.2 Controller performance under Mexican hat profile

The controller performance under a Mexican hat wind profile is analysed in Fig. 10. This profile introduces a temporally localized high-energy gust (Addison 2002). A pronounced acceleration peak followed by symmetric deceleration is observed in Fig. 10(a). Unlike stochastic excitation, oscillations are not persistent but concentrated around the gust interval. The estimated speed tracks this rapid transient without overshoot or oscillatory correction. When rotor resistance is increased, a peak overshoot of 13.27%, followed by a settling time of approximately 0.31 s, appears. The settling time reflects the slower mechanical dynamics compared to the electrical subsystem. The estimated speed does not exhibit overshoot or transient deviation, remaining tightly aligned with the reference trajectory. This confirms that the sliding-mode observer preserves estimation stability despite severe parametric perturbation. After adaptation, real speed rapidly realigns with reference. The torque response illustrated in Fig. 10(b) shows a

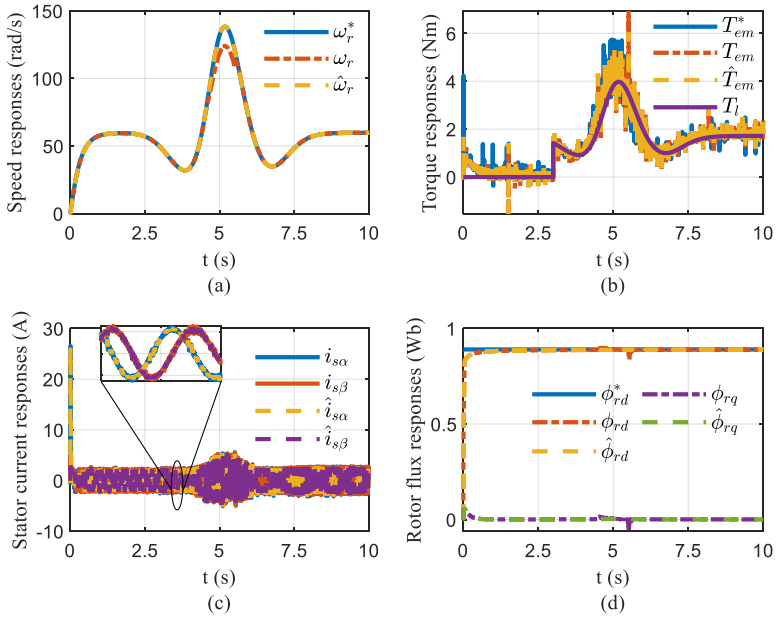

Fig. 10 Dynamic responses of the wind turbine simulator under the *Mexican* hat wind profile: (a) reference, real, and estimated rotor speed; (b) reference, real and estimated electromagnetic torque with load torque; (c) real and estimated stator currents in the α–β reference frame; (d) reference, real, and estimated rotor flux in the d–q reference frame.

sharp transient peak synchronized with the gust excitation. The torque imbalance induced by rotor resistance variation is clearly visible, reflecting the temporary detuning of flux orientation. Once the reactive power–based adaptation is enabled, the electromagnetic torque rapidly realigns with its reference value. Quantitatively, after adaptation, torque error falls below 5%, indicating effective restoration of electromagnetic equilibrium. The estimated torque remains stable throughout the disturbance, demonstrating that the observer is not destabilized by the modified rotor time constant and that adaptation primarily compensates the physical variables rather than stabilizing the estimator. During the gust peak, stator current amplitude (Fig. 10(c)) increases significantly to supply the required electromagnetic torque (Zerzeri *et al.* 2026). The transient current rise reflects enhanced energy conversion from aerodynamic input to electromagnetic output. Despite the abrupt disturbance, current waveforms remain sinusoidal and free from distortion, confirming the modulation robustness of the 4S-VSI. After activation of adaptation, stator current error decreases below 3%, indicating that flux orientation and torque production are fully restored. In contrast to the mechanical speed response, the rotor flux remains only weakly affected by the disturbance (Fig. 10(d)). The flux exhibits a limited overshoot of 1.85%, with an almost instantaneous settling time on the order of 10^{-4} s. This rapid electrical recovery confirms the inherently faster dynamics of the electromagnetic subsystem compared to the mechanical one, as well as the effectiveness of the flux–torque decoupling ensured by the FOC structure. The estimated flux does not exhibit overshoot or transient deviation, remaining stable throughout the disturbance. After adaptation is enabled, the rotor flux deviation becomes practically zero. The structured, localized excitation enhances observability without inducing persistent disturbance, which explains the superior performance observed for this profile. Across all three wind profiles, the estimated quantities remain closely aligned with both reference and real values. Even under severe rotor resistance variation and dynamic excitation, no estimator divergence or oscillatory instability is observed. The adaptation mechanism primarily realigns the physical system variables, while the sliding-mode observer maintains stable state reconstruction throughout the operating range.

4.3 WTS qualitative and quantitative discussion

4.3.1. Qualitative Error and Waveform Analysis

To evaluate the accuracy of the proposed wind turbine simulator under varying operating conditions, the relative errors of the main electrical and mechanical variables are analyzed for the three wind profiles. The mathematical definition of the relative error is provided in Appendix B (Eq. B.2). The corresponding results are illustrated in Figs. 11–13. During unloaded start-up (0–3 s), the rotor speed error remains practically zero for all wind profiles, indicating fast observer convergence and effective flux–torque decoupling. Electromagnetic torque error exhibits transient oscillations due to the absence of load torque and the dominance of acceleration dynamics. These oscillations are more pronounced under the stochastic profile because of its broadband excitation content (Larsen *et al.* 2008; International Electrotechnical Commission 2019). The stator current error increases with operating speed and excitation frequency, reaching approximately 2% at 25 rad/s, 5% at 50 rad/s, and 9% at 100 rad/s.

This trend reflects the higher electromagnetic energy exchange required at elevated speeds. Rotor flux error remains close to zero, confirming stable flux estimation and accurate orientation. When mechanical load is applied under nominal

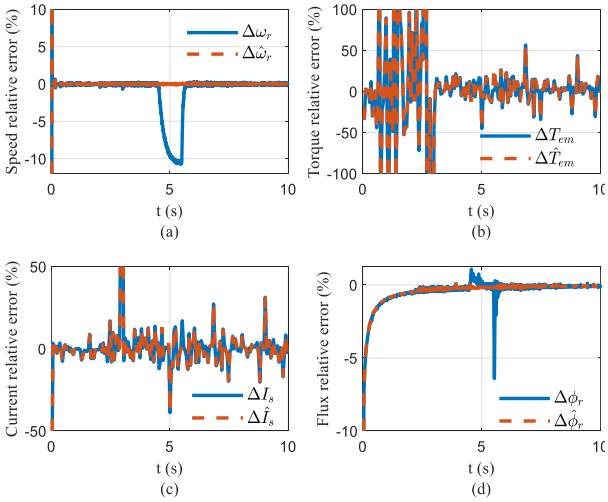

Fig. 7 Relative errors between real WTS quantities in continuous line and estimated quantities in dashed line under linear/constant wind profile: (a) Speed; (b) Torque; (c) Stator current module (d) Rotor flux module.

parameters (3–4.5 s), the system enters aerodynamic equilibrium. Speed tracking accuracy remains within 1% for all profiles. Torque error stabilizes around 3% for the linear profile, 6% for the Mexican Hat profile, and 10% for the stochastic profile. The higher deviation observed in the stochastic case is attributable to turbulence-induced irregular excitation, which perturbs instantaneous torque balance. Current error increases at higher speeds (up to 15% at 130 rad/s), consistent with increased electromagnetic demand, while rotor flux error remains below 2%.

A 100% rotor resistance increase introduced during loaded operation produces a clear degradation in physical variable alignment. Speed error reaches up to 10%, and torque error approaches 20%, reflecting the disturbance of the rotor time constant and the resulting torque imbalance. The actual rotor flux error increases to about 3%, whereas the estimated flux remains nearly unaffected (below 1%), confirming the intrinsic robustness of the sliding-mode observer to parameter mismatch. Current error rises to approximately 15% at low

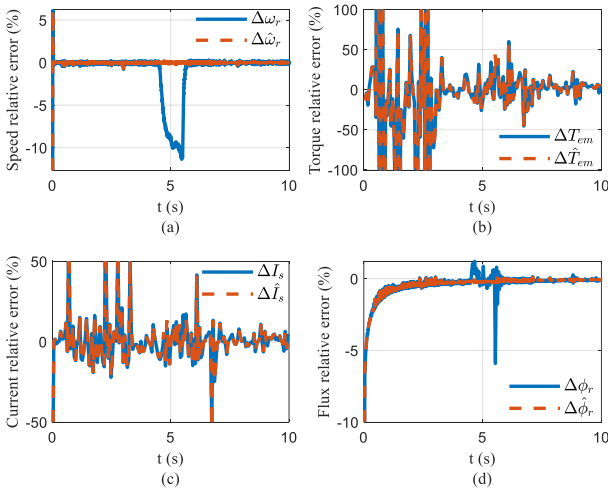

Fig. 8 Relative errors between real WTS quantities in continuous line and estimated quantities in dashed line under stochastic wind profile: (a) Speed; (b) Torque; (c) Stator current module (d) Rotor flux module.

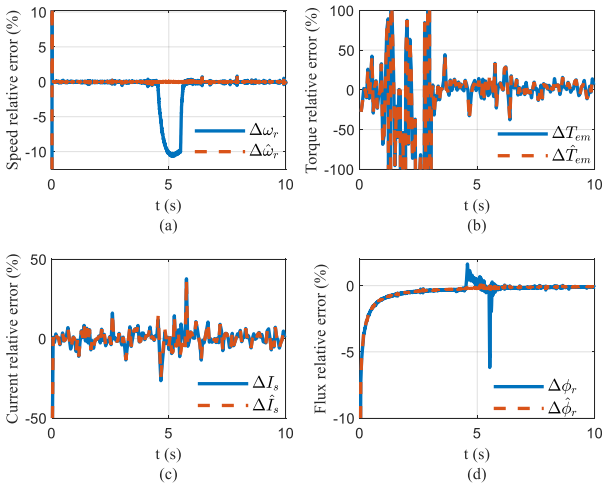

Fig. 9 Relative errors between real WTS quantities in continuous line and estimated quantities in dashed line under Mexican hat wind profile: (a) Speed; (b) Torque; (c) Stator current module (d) Rotor flux module.

speed and 7% at high speed, highlighting the sensitivity of electromagnetic torque production to rotor resistance variation.

Once the reactive power–based adaptation is activated, the real machine variables progressively realign with their reference trajectories. Speed error returns to nearly zero, torque error falls below 5%, current error decreases below 3%, and flux deviation becomes negligible. Importantly, the estimated quantities remain stable throughout the disturbance and recovery phases, demonstrating that the observer maintains robustness while the adaptation mechanism restores physical model consistency.

4.3.2. Quantitative performance evaluation

To complement the waveform analysis, a quantitative assessment based on Mean Absolute Error (MAE) and Root Mean Square Error (RMSE) indices is provided in Table 1. Their mathematical definitions are given in Appendix B (Eqs. B.3 and B.4). These metrics are calculated for rotor speed and electromagnetic torque during loaded operation under nominal conditions, rotor resistance variation, and adaptive compensation.

Under nominal conditions, the Mexican Hat profile yields the lowest MAE and RMSE values. This behavior can be physically interpreted through its structured transient nature: the localized gust-like excitation introduces sufficient dynamic richness to satisfy observer excitation requirements without injecting excessive broadband turbulence. As a result, flux alignment and torque estimation consistency are enhanced.

When rotor resistance is doubled, both MAE and RMSE increase for all wind profiles, confirming the sensitivity of sensorless schemes to parametric drift. The degradation is most pronounced under stochastic excitation due to its irregular spectral content, which amplifies transient torque imbalance. After enabling reactive power–based adaptation, the MAE and RMSE values decrease significantly across all profiles. The Mexican Hat case again exhibits the lowest errors, indicating that controlled transient excitation can improve estimation quality while preserving steady-state stability.

4.3.3. Quantitative analysis between 4S-VSI and 6S-VSI topologies

To assess the energetic and structural efficiency of the proposed four-switch inverter, a quantitative comparison is conducted with a conventional six-switch VSI operating under identical PWM carrier frequency and modulation conditions. The analysis focuses on the steady-state interval (5.5–6 s), where dynamic transients do not influence the switching statistics. The results are summarized in Table 2. Although both converters employ the same carrier frequency, the 4S-VSI inherently requires fewer switching transitions due to its reduced number of active semiconductor devices. The equivalent switching frequency decreases from 44.89 kHz in the 6S-VSI to 25.72 kHz in the 4S-VSI, corresponding to an approximately 43% reduction in total commutations. From a physical standpoint, switching losses are directly proportional to the number of commutation events and the associated voltage–current overlap during device transitions. Therefore, the observed reduction translates into a substantial decrease in switching losses and thermal stress. Lower commutation density also mitigates electromagnetic interference and improves converter reliability. Importantly, this reduction in switching activity does not compromise control performance. As demonstrated in the previous subsections, observer convergence, torque tracking accuracy, and flux regulation remain comparable to those achieved with conventional six-switch architectures. The 4S-VSI therefore achieves a favorable trade-off between dynamic

Table 2
Comparison of commutation number between 4S-VSI and 6S-VSI topologies.

Topology	Number of switches	Commutations per switch	Total commutations	Equivalent switching frequency
6S-VSI	6	S1: 3741 S2: 3741 S3: 3741 S4: 3741 S5: 3742 S6: 3742	22,448	44.89 kHz
4S-VSI	4	S1: 3301 S2: 3129 S3: 3301 S4: 3129	12,860	25.72 kHz

Table 1.
Quantitative performance evaluation of the proposed WTS under different wind profiles and operating conditions: MAE and RMSE of speed and electromagnetic torque.

Wind profile	Quantity	Nominal (3–4.5 s)		R_r variation (4.5–5.5 s)		With adaptation (5.5–10 s)	
		MAE	***RMSE***	***MAE***	***RMSE***	***MAE***	***RMSE***
Linear/constant	Speed (rad/s)	0.0697	0.0944	0.0705	0.0942	0.0594	0.0858
	Torque (Nm)	0.3581	0.4970	0.3791	0.5282	0.3109	0.4662
Mexican hat	Speed (rad/s)	0.0125	0.0279	0.0718	0.0975	0.0176	0.0399
	Torque (Nm)	0.1056	0.1733	0.3809	0.5289	0.1303	0.2362
Stochastic	Speed (rad/s)	0.0583	0.0899	0.0545	0.0772	0.0477	0.0751
	Torque (Nm)	0.3123	0.4485	0.3084	0.4443	0.2679	0.4160

performance, power loss reduction, hardware simplification, and implementation cost. This makes it particularly suitable for laboratory-scale wind turbine emulators and real-time simulation platforms, where efficiency and structural simplicity are critical design criteria.

4.3.4. Performance of Mexican Hat profile under parameter variations

To further strengthen the robustness assessment of the proposed control strategy, an additional sensitivity analysis is carried out by introducing a stator resistance variation under the Mexican Hat wind profile, which previously demonstrated the most favorable excitation–estimation balance. This profile is retained to isolate parameter sensitivity from excessive turbulence-induced disturbances. The simulation timeline follows the same operating sequence previously defined: unloaded start-up (0–3 s), nominal loaded operation (3–4.5 s), a 100% rotor resistance variation (4.5–5.5 s) compensated by the reactive power–based adaptation, and steady-state operation thereafter. At $t = 6$s, an abrupt increase of +50% in stator resistance is applied while maintaining the reactive power adaptation for rotor resistance. As shown in Fig. 14(a), the stator resistance adaptation effectively tracks the imposed variation, ensuring stable system operation.

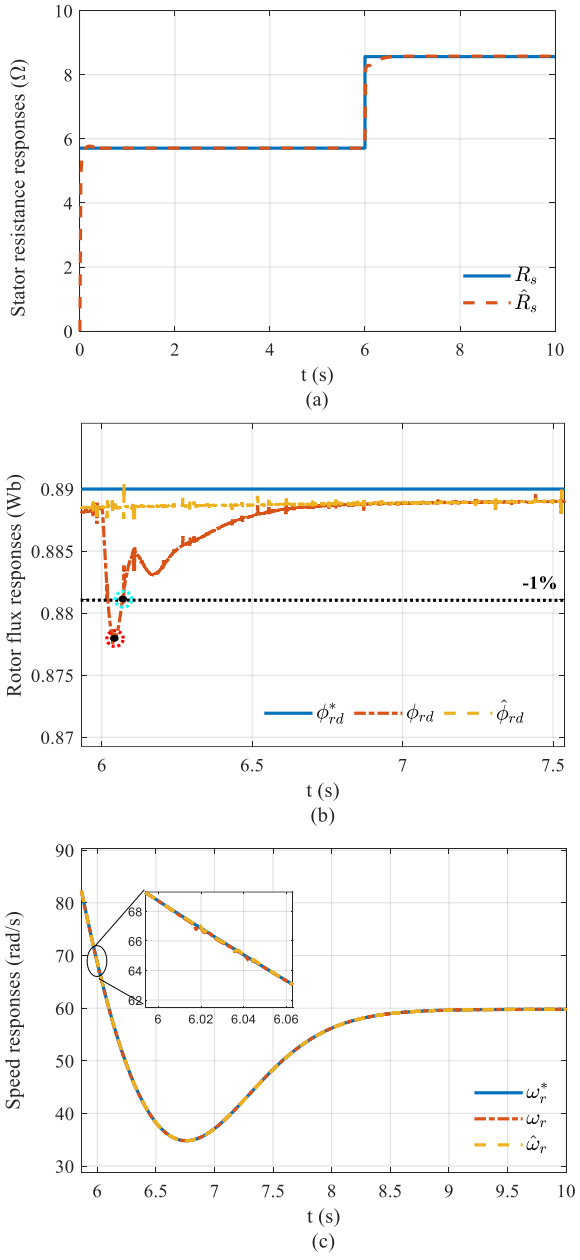

Fig. 14. Performance of the proposed sensorless control strategy under combined parameter variations using the Mexican Hat wind profile: (a) Real and estimated stator resistance following a sudden 50% variation applied at $t = 6$s; (b) real, estimated, and reference rotor flux responses; (c) real, estimated, and reference mechanical speed responses.

The rotor flux response presented in Fig. 14(b) exhibits a limited undershoot of approximately 1.37%, with a settling time within ±1% of about 0.07 s. This rapid electrical stabilization reflects the fast time constant of flux dynamics and the effectiveness of the decoupled control structure. Notably, the estimated flux components remain unaffected by the stator resistance disturbance, indicating strong observer resilience to parameter uncertainty. The mechanical speed response depicted in Fig. 14(c) shows only a slight transient deviation at the instant of parameter variation. Due to mechanical inertia and electromagnetic torque regulation, the deviation is quickly attenuated without overshoot, and the speed converges smoothly to its reference trajectory. Throughout this perturbation, the estimated flux and speed remain stable and aligned with the reference signals, confirming the resilience of the sliding-mode observer under simultaneous electrical parameter drift. These results demonstrate that the proposed control–observer architecture maintains stable operation under combined rotor and stator resistance uncertainties. The electrical subsystem absorbs parametric perturbations within a short time scale, while the mechanical dynamics remain weakly affected due to inertia filtering. The Mexican Hat excitation further ensures sufficient dynamic richness for state reconstruction without introducing destabilizing broadband noise.

4.4 Comparative discussion with recent SMO-based approaches

To place the proposed observer performance under parametric drift in perspective, a comparative discussion with recent SMO-based approaches reported in the literature is provided. In Zaky *et al.* (2018), a +50% stator resistance variation applied at low-speed leads to significant transient deviations, with reported speed overshoot exceeding 60% and a settling time on the order of 0.3 s. By contrast, under a comparable stator resistance variation magnitude, the proposed observer exhibits no observable speed overshoot and a negligible settling time, as shown in Fig. 14(c).

A direct comparison can also be drawn with the recent work of Zerzeri *et al.* (2024), where a wind turbine emulator based on a single-phase induction motor supplied by a 4S-VSI is combined with a sliding-mode control strategy and a Lyapunov-based rotor resistance adaptation mechanism. In both approaches, the observer demonstrates effective convergence under rotor and stator resistance variations, confirming the suitability of sliding-mode techniques for sensorless wind turbine emulation. Compared with the results reported in Zerzeri *et al.* (2024), the proposed method exhibits slightly improved transient behavior, particularly in terms of reduced speed deviation and faster recovery following parameter perturbations. Moreover, the reactive power–based adaptation mechanism adopted in this work significantly reduces computational complexity compared to Lyapunov-based adaptation laws, while preserving observer robustness.

Regarding inverter topology, Kumar *et al*. (2024) analyze wind turbine emulators based on conventional two-level VSI configurations, achieving satisfactory estimation accuracy at the expense of increased switching activity and converter complexity. As demonstrated in Section 4.3.3, the proposed 4S-VSI topology achieves comparable estimation accuracy while reducing switching events by approximately 43%, which directly translates into lower switching losses and reduced hardware cost. These results confirm that the reduced-switch architecture does not compromise observer robustness and represents an efficient solution for cost-effective wind turbine emulation.

5. Conclusion

This paper has presented a robust software-based wind turbine simulator built on a three-phase induction motor supplied by a reduced-switch four-switch voltage source inverter (4S-VSI). The proposed architecture integrates rotor field-oriented control, space vector modulation, and a sliding-mode observer to ensure accurate sensorless estimation of rotor speed and flux while minimizing hardware complexity.

The simulator has been validated under linear/constant, stochastic, and Mexican Hat wind profiles representative of quasi-stationary, turbulent, and gust-type atmospheric conditions. The structured excitation introduced by the Mexican Hat profile proved particularly suitable for analyzing observer convergence under dynamic disturbances. Under nominal loaded operation, speed tracking error remained below 1%, torque error below 6%, and rotor flux deviation below 2%. When a severe +100% rotor resistance variation was introduced, transient speed deviation reached 10% and torque error approached 20%; however, the estimated quantities remained stable. After activation of the reactive power–based adaptation mechanism, speed error returned to nearly zero, torque error was reduced below 5%, current error below 3%, and flux deviation became negligible, confirming rapid convergence and strong robustness against parametric drift. A quantitative comparison with a conventional six-switch VSI demonstrated that the proposed 4S-VSI reduces switching activity by approximately 43%, leading to lower switching losses and reduced converter complexity without degrading dynamic performance or observer accuracy.

The proposed emulator achieves a favorable compromise between dynamic fidelity, observer robustness, switching loss reduction, and computational simplicity. Future work will extend the platform toward hardware-in-the-loop implementation to validate real-time performance under practical operating constraints and further support cost-effective wind energy system development.

References

Addison, P. (2002). The Illustrated Wavelet Transform Handbook, CRC. *Press,*.

Allouche, M., Abderrahim, S., Ben Zina, H., et al. (2019). A novel fuzzy control strategy for maximum power point tracking of wind energy conversion system. *International Journal of Smart Grid* 3, 120–127.

Battaiotto, P.E., Mantz, R.J., Puleston, P.F. (1996). A wind turbine emulator based on a dual dsp processor system. *Control Engineering Practice* 4(9), 1261–1266; https://doi.org/10.1016/0967-0661(96)00132-3

Bednarz, S. A., & Dybkowski, M. (2019). Estimation of the induction motor stator and rotor resistance using active and reactive power based model reference adaptive system estimator. *Applied Sciences*, *9*(23), 5145. https://doi.org/10.3390/app9235145

Benaaouinate, L., Khafallah, M., Mesbahi, A. (2017). Emulation of a wind turbine with a dc motor controlled by fuzzy logic controller. *In: Proceedings of Engineering and Technology (PET)*, vol. 20, pp. 97–101.

Benchaib, A., Rachid, A., Audrezet, E., & Tadjine, M. (2002). Real-time sliding-mode observer and control of an induction motor. *IEEE Transactions on Industrial Electronics*, *46*(1), 128-138; https://doi.org/10.1109/41.744404

Boutabba, T., Benlaloui, I., Mechnane, F., Elzein, I. M., Ammar, M., & Mahmoud, M. M. (2025). Design of a Small Wind Turbine Emulator for Testing Power Converters Using dSPACE 1104. *International Journal of Robotics and Control Systems*, *5*(2), 698-712; https://doi.org/10.31763/ijrcs.v5i2.1685

Che, H., Tao, Y., Yang, J., & Zhao, Z. (2023). A New SMO for Speed Estimation of Sensorless Induction Motor Drives at Zero and Low Speed. *IEEJ Transactions on Electrical and Electronic Engineering*, *18*(4), 559-567; https://doi.org/10.1002/tee.23754

Chen, J., & Huang, J. (2017). Stable simultaneous stator and rotor resistances identification for speed sensorless IM drives: Review and new results. *IEEE Transactions on Power Electronics*, *33*(10), 8695-8709; https://doi.org/10.1109/TPEL.2017.2785330

Chinchilla, M., Arnaltes, S., Rodriguez-Amenedo, J.L. (2004). Laboratory setup for wind turbine emulation. *In: IEEE International Conference on Industrial Technology (ICIT)*, Hammamet, Tunisia.

De Oliveira, J.R., Andreoli, A.L. (2021). Wind turbine emulator: A tool for experimental and computational study. *IEEE Latin America Transactions* 19(11), 1832–1839; https://doi.org/10.1109/TLA.2021.9475616

Donnou, H.E.V., Akpo, A.B., Houngue, G.H. and Kounouhewa, B.B. (2020) Assessment of IEC Normal Turbulence Model and Modelling of the Wind Turbulence Intensity for Small Wind Turbine Design in Tropical Area: Case of the Coastal Region of Benin. *International Journal of Renewable Energy Development*, 9(2), 263-286; https://doi.org/10.14710/ijred.9.2.263-286

Farag, W.A. (2023). Accurate wind energy harvest assessment using a comprehensive ultra-large-wind-turbine emulation. *Journal of Engineering Research* 11(3), 123–133; https://doi.org/10.1016/j.jer.2023.100096

Farag, W., El-Hosary, M., Kamel, A. (2017). A comparative study and analysis of different yaw control strategies for large wind turbines. *In: International Conference on Advanced Control Circuits Systems (ACCS)*, Alexandria, Egypt.

Guenoukpati, A., Salami, A.A., Kodjo, M.K., and Napo,K. (2020) Estimating Weibull Parameters for Wind Energy Applications Using Seven Numerical Methods: Case studies of Three Coastal Sites in West Africa. *International Journal of Renewable Energy Development*, 9(2), 217-226; https://doi.org/10.14710/ijred.9.2.217-226

Hassan, A., Bazzi, A. M., Jensen, F., & Karaki, S. H. (2025). Analysis and Comparison of Nonlinear Kalman Filters for Sensorless Induction Motor Drives To Achieve Multiple Model Estimation. *IEEE Transactions on Industry Applications* 61(4), pp. 6422-6433; https://doi.org/10.1109/TIA.2025.3546902

Hassan, H.M., Farag, W.A., Shawkey, M. (2011). Designing pitch controller for large wind turbines via lmi techniques. *Energy Procedia* 12, 808–818; https://doi.org/10.1016/j.egypro.2011.10.107

Heier, S. (2014). *Grid integration of wind energy: onshore and offshore conversion systems*. John Wiley & Sons.

Hemeida, A.M., Mahgoub, O.A., Farag, W.A. (2013). Design of a comprehensive 5mw direct-driven pmsg wind turbine emulator using fast nonlinear wind turbine model. *22 International Journal of Automation and Control Engineering* 2(4), 190–196.

IEA. (2024). World Energy Outlook 2024. https://www.iea.org/reports/world-energy-outlook-2024. Accessed: 2025-06-26.

International Electrotechnical Commission. (2019). Wind Turbine Generator Systems Part 1: Design Requirements. *4th ed, IEC 61400-1*.

IRENA. (2024). Renewable Capacity Statistics 2024. https://www.irena.org/Publications/2024/Mar/Renewable-capacity-statistics-2024. Accessed: 2025-06-26.

Jing, B., Qun, L., Qiang, L., Zaiyu, C., Yuchong, H., Minghui, Y. (2023). Inertia compensation for wind turbine emulator based on anticipation deviation suppression. *Electric Power Systems Research* 224, 109751.

Jnayah, S., Zerzeri, M., Moussa, I., & Khedher, A. (2023, September). Wind Turbine Emulator Using Three-Level Inverter-Fed Induction

Motor Drive Controlled Through DTC Strategy. In *International Conference on Green Energy Conversion System* (pp. 93-103). Singapore: Springer Nature Singapore; https://doi.org/10.1007/978-981-97-6148-7_10

Kathiresan, C.A., PandiaRajan, J., Sivaprakash, A. (2020). An adaptive feed-forward phase locked loop for grid synchronization of renewable energy systems under wide frequency deviations. *Sustainability* 12(17), 7048; https://doi.org/10.3390/su12177048

Khan, A., Aragon, D.A., Seyedmahmoudian, M., Mekhilef, S., Stojcevski, A. (2024). Recent advancements in wind turbine emulator technologies: Trends, challenges and future directions. *International Journal of Electrical Power & Energy Systems* 156, 109740.

Kojabadi, H.M., Chang, L. (2004). A novel steady state wind turbine simulator using an inverter controlled induction motor. Wind Engineering 28(4), 433–443; https://doi.org/10.1260/0309524042886

Korzonek, M., Tarchala, G., & Orlowska-Kowalska, T. (2019). A review on MRAS-type speed estimators for reliable and efficient induction motor drives. *ISA transactions*, *93*, 1-13; https://doi.org/10.1016/j.isatra.2019.03.022

Kouadria, S., Belfedhal, S., Berkouk, E.M. (2013). Development of real time wind turbine emulator based on dc motor controlled by pi regulator. *In: IEEE 8th International Conference and Exhibition on Ecological Vehicles and Renewable Energies (EVER)*, Monte Carlo, Monaco.

Kumar, G. N., Sai, R. V., Reddy, T. M., Shajid, S. K., & Boora, K. (2024). Emulation of Wind Turbine System Using Fuzzy Controller-Based Vector Controlled Induction Motor Drive. *Journal of Modern Technology*, 38-46. https://doi.org/10.71426/jmt.v1.i1.pp3-46

Kumar, R., Das, S., Syam, P., & Chattopadhyay, A. K. (2015). Review on model reference adaptive system for sensorless vector control of induction motor drives. *IET Electric Power Applications*, *9*(7), 496-511; https://doi.org/10.1049/iet-epa.2014.0220

Larsen, G. C., & Hansen, K. S. (2008). Rational calibration of four IEC 61400-1 extreme external conditions. *Wind Energy: An International Journal for Progress and Applications in Wind Power Conversion Technology*, *11*(6), 685-702, https://doi.org/10.1002/we.302Digital Object Identifier (DOI)

Li, J., Xu, L., & Zhang, Z. (2005). An adaptive sliding-mode observer for induction motor sensorless speed control. *IEEE Transactions on Industry Applications*, *41*(4), 1039-1046; https://doi.org/10.1109/TIA.2005.851585

Lu, L., Xie, Z., Zhang, X., et al. (2012). A dynamic wind turbine simulator of the wind turbine generator system. *In: IEEE 2nd International Conference on Intelligent System Design and Engineering Application (ISDEA)*, Sanya, China, pp. 728–731.

Maeda, T., Kamada, Y., & Li, Q. A. (2017). Experiment and Simulation Effects of Cyclic Pitch Control on Performance of Horizontal Axis Wind Turbine. *International Journal of Renewable Energy Development 6*(2), 119-125; https://doi.org/10.14710/ijred.6.2.119-125

Maheshwari, Z., Kengne, K., Bhat, O. (2023) . A comprehensive review on wind turbine emulators. *Renewable and Sustainable Energy Reviews* 180, 113297; https://doi.org/10.1016/j.rser.2023.11329723

Moaveni, B., Masoumi, Z., & Rahmani, P. (2023). Introducing improved iterated extended kalman filter (iiekf) to estimate the rotor rotational speed, rotor and stator resistances of induction motors. *IEEE Access*, *11, pp. 17584-17593*; https://doi.org/17584-17593. 10.1109/ACCESS.2023.3244830

Merabet, A., Tawfique Khandker, A., Islam, M.A. (2014). Wind turbine emulator using opal-rt real-time hil/rcp laboratory. *In: IEEE 26th International Conference on Microelectronics (ICM)*, Doha, Qatar. https://doi.org/10.1109/ICM.2014.7071839

Météo-France (2019). *Hourly wind speed data from Brest-Guipavas meteorological station (1995–2019).* French National Meteorological Service, Toulouse, France. Available at: https://donneespubliques.meteofrance.fr

Mohan, H., Pathak, M. K., and Dwivedi, S. K. (2020): Sensorless Control of Electric Drives – A Technological Review. *IETE Technical Review*, *37*(5), 504-528; https://doi.org/10.1080/02564602.2019.1662738

Moussa, I., Bouallegue, A., Khedher, A. (2019). New wind turbine emulator based on dc machine: hardware implementation using fpga board for an open-loop operation. *IET Circuits, Devices & Systems* 13, 896–902; https://doi.org/10.1049/iet-cds.2018.5530

Moussa, I., Zerzeri, M., & Khedher, A. (2022, October). Robust WTE sensorless design based on soft-VSI structure for three-phase IM drive using sliding mode observer controller. In *2022 IEEE International Conference on Electrical Sciences and Technologies in Maghreb (CISTEM)* (Vol. 4, pp. 1-7). IEEE. https://doi.org/10.1109/CISTEM55808.2022.10044004

Moussa, I., & Khedher, A. (2022). Soft-switching inverter investigation for three-phase IM drive as wind turbine emulator design. *Microelectronics Reliability*, *138*, 114722; https://doi.org/10.1016/j.microrel.2022.114722

Moussa, I., & Khedher, A. (2022). Wind turbine emulator controlled through field programmable gate array: modeling, analysis, and design. In *Recent Advances in Renewable Energy Technologies* (pp. 251-283). Academic Press; https://doi.org/10.1016/B978-0-12-823532-4.00005-7

Morfin Onofre, A., Ruiz-Cruz, R., Hernández Jesus, I., et al. (2021). Real-time sensor-less robust velocity controller applied to a dc-motor for emulating a wind turbine. *Energies* 14(4), 868; https://doi.org/10.3390/en14040868

Nair, R., Narayanan, G. (2020). Emulation of wind turbine system using vector controlled induction motor drive. *IEEE Transactions on Industry Applications* 56(4), 4124–4133; https://doi.org/10.1109/TIA.2020.2987993

Rajendran, S., Diaz, M., Devi, V.K., Jena, D., Travieso, J.C., Rodriguez, J. (2023). Wind turbine emulators—a review. Processes 11(3), 747; https://doi.org/10.3390/pr11030747

Rubinstein, R. Y., & Kroese, D. P. (2016). Simulation and the Monte Carlo method. *John Wiley & Sons*.

Sebestyén, V. (2021). Environmental impact networks of renewable energy power plants. *Renewable and Sustainable Energy Reviews* 151, 111626; https://doi.org/10.1016/j.rser.2021.111626

Satish Kumar, P., Chandrasena, R.P.S., Victor Sam Moses Babu, K. (2022). Design and implementation of wind turbine emulator using fpga for stand-alone applications. *International Journal of Ambient Energy* 43(1), 2397–2409; https://doi.org/10.1080/01430750.2020.1736152

Salami, A.A., Ouedraogo, S., Kodjo,K.M., and Ajavon, A. S.A., (2022), Influence of the random data sampling in estimation of wind speed resource: Case study. *Int. J. Renew. Energy Dev.*, 11(1), 133-143; https://doi.org/10.14710/ijred.2022.38511

Torrence, C., & Compo, G. P. (1998). A practical guide to wavelet analysis. *Bulletin of the American Meteorological society*, *79*(1), 61-78.

Tu, X., Hou, X., Zhao, J., Yan, S., & Xiong, Y. (2023). Speed identification of speed sensorless linear induction motor based on MRAS. *CES Transactions on Electrical Machines and Systems*, *7*(3), 294-300; https://doi.org/10.30941/CESTEMS.2023.00032

Verma, V., Chakraborty, C., Maiti, S., & Hori, Y. (2013). Speed sensorless vector controlled induction motor drive using single current sensor. *IEEE Transactions on Energy Conversion*, *28*(4), 938-950; https://doi.org/10.1109/TEC.2013.2273935

Wang, T., Wang, B., Yu, Y., & Xu, D. (2023). Discrete sliding-mode-based MRAS for speed-sensorless induction motor drives in the high-speed range. *IEEE Transactions on Power Electronics*, *38*(5), 5777-5790; https://doi.org/10.1109/TPEL.2023.3236024

WWEA. (2024). WWEA Annual Report 2024: A Challenging Year for Windpower. https://www.wwindea.org/AnnualReport2024. Accessed: 2025-06-26

WWEA. (2024). WWEA podcast: Wind Power Around the World – Opportunities and Challenges. https://wwindea.org/worldwide-wind-capacity-reaches744-gigawatts. Accessed: 2025-06-26

Yan, J., Feng, Y., Dong, J. (2016). Study on dynamic characteristic of wind turbine emulator based on pmsm. *Renewable Energy* 97, 731–736; https://doi.org/10.1016/j.renene.2016.06.034

Yang, Z., Ding, Q., Sun, X., Lu, C., & Zhu, H. (2022). Speed sensorless control of a bearingless induction motor based on sliding mode observer and phase-locked loop. *ISA transactions*, *123*, 346-356; https://doi.org/10.1016/j.isatra.2021.05.041

Yildiz, R., Barut, M., & DEMİR, R. (2024). Online stator and rotor resistance estimations of IM by using EKF. *Pamukkale University Journal of Engineering Sciences*, *30*(6); https://doi.org/10.1177/01423312231160582

Zaky, M. S., Metwaly, M. K., Azazi, H. Z., & Deraz, S. A. (2018). A new adaptive SMO for speed estimation of sensorless induction motor drives at zero and very low frequencies. *IEEE Transactions on*

Industrial Electronics, *65*(9), 6901-6911; https://doi.org/10.1109/TIE.2018.2793206

Zerzeri, M., Moussa, I., & Khedher, A. (2024, April). Adaptive Sliding-Mode Observer for FOC of IM Drives Fed by Soft-VSI Topology: Wind Turbine Emulator Application. In *2024 IEEE International Conference on Advanced Systems and Emergent Technologies (IC_ASET)* (pp. 1-6). IEEE; https://doi.org/10.1109/IC_ASET61847.2024.10596156

Zerzeri, M., Moussa, I., & Khedher, A. (2024). Sliding mode control for wind turbine emulator based on advanced space vector modulation technique for two-phase induction motor drive. *IETE Journal of Research*, *70*(2), 1800-1813; https://doi.org/10.1080/03772063.2022.2154711

Zerzeri, M., Moussa, I., & Khedher, A. (2026). A Software-Implemented Wind Turbine Emulator Using a Robust Sensorless Soft-VSI Induction Motor Drive with STA-Based Flux Observation and MRAS Speed Estimation. *Automation*, *7*(1), 30. https://doi.org/10.3390/automation7010030

Zhao, K., Song, B., Tang, X., & Zhou, X. (2025). Second-Order Complex-Coefficient Flux Observer with Stator Resistance Estimation for Induction Motor Sensorless Drives. *Machines*, *13*(9), 845; https://doi.org/10.3390/machines13090845

Appendices

Appendix A. System Parameters and Simulation Data

Table A1
Wind Parameters

Wind profile	Value
Mexican hat	Mean speed: 6 m/s Burst speed: 11 m/s Burst core time: 5 s Shape factor: 0.4
Sinusoidal	$k_1 = 2$, $k_2 = -1.75$, $k_3 = 1.5$, $k_4 = -1.25$, $k_5 = 1$, $k_6 = 0.5$, $k_7 = 0.25$; $a_1 = 1$, $a_2 = 3$, $a_3 = 5$, $a_4 = 10$, $a_5 = 20$, $a_6 = 50$, $a_7 = 100$

Table A2
Wind Turbine Parameters

Parameter	Value	Parameter	Value
Rotor radius	3.61 m	Pitch angle	3°
Gearbox ratio	13	Cut-in wind speed	4.2 m/s
Air density	1.225 kg/m³	Power coefficient	0.52

Table A3
IM Simulation Parameters

Parameter	Value	Parameter	Value
R_r	4.28 Ω	L_r	0.464 H
R_s	5.72 Ω	L_s	0.464 H
M	0.44 H	f	0.002 N·m·s·rad^{-1}
n_p	2	J	0.0049 kg·m²

Appendix B. Performance indicators

B.1. Rotor resistance variation model

In order to emulate realistic thermal and parametric effects in the induction machine, the rotor resistance is varied according to a smooth exponential law, expressed as:

$$R_r(t) = R_{r_0} + \left(R_{r_0} \left[1 - e^{-2(t-2)} \right] \right) \quad \text{(B.1)}$$

Where $R_{r_0} = 4.28\Omega$.

B.2. Relative error definitions

To quantify the deviation between reference (X^*), real (X), and estimated ($\hat{X}$) quantities, the relative error indices are defined as follows:

$$\begin{cases} \Delta X(\%) = \dfrac{X^* - \hat{X}}{X^*} \times 100 \\ \Delta \hat{X}(\%) = \dfrac{\hat{X} - X}{\hat{X}} \times 100 \end{cases} \quad \text{(B.2)}$$

Where X represents ω_r , T_{em} , I_s and ϕ_r respectively. I_s and ϕ_r are the stator current and rotor flux modules.

B.3. MAE and RMSE performance metrics

In addition to relative error analysis, MAE and RMSE indices are employed to evaluate the estimation accuracy over the considered operating intervals:

$$MAE = \frac{1}{N} \sum_{k=1}^{N} \left| X^*(k) - \hat{X}(k) \right| \quad \text{(B.3)}$$

$$RMSE = \sqrt{\frac{1}{N} \sum_{k=1}^{N} \left(X^*(k) - \hat{X}(k) \right)^2} \quad \text{(B.4)}$$

Where X^* denotes the reference value, $\hat{X}$ is the estimated value, and N represents the number of samples within the considered evaluation interval.

Appendix C. Mechanical Model and Inertia Compensation Derivation

The mechanical behavior of the real WTGS is described by rotational dynamics as follows:

$$\boldsymbol{J_{t-g}\frac{d\Omega_t}{dt} = T_t - T_g} \quad \text{(C.1)}$$

$$\boldsymbol{J_g\frac{d\Omega_g}{dt} = T_g - T_l} \quad \text{(C.2)}$$

Where, J_{t-g} is the combined inertia of the turbine–generator system, Ω_g is the generator mechanical speed, T_g is the generator torque, J_g is the generator inertia and T_l is the load torque.
For the induction motor used in the emulator, the rotational dynamics are expressed as:

$$J_{m-g}\frac{d\Omega_{emu}}{dt} = T_{m-g} - T_l \quad \text{(C.3)}$$

Where J_{m-g} is the equivalent inertia of the motor–generator subsystem and T_{m-g} is the torque generated by the emulator.
Since $J_{m-g} \neq J_{t-g}$, a torque compensation mechanism is required to ensure equivalent dynamic behavior. The compensated torque is defined as:

$$T_{m-g} = T_g + \Delta T_{compensation} \quad \text{(C.4)}$$

The inertia error compensation term is given by:

$$\Delta T_{compensation} = K_{inertia}\left(J_{t-g}\frac{d\Omega_t}{dt} - J_{m-g}\frac{d\Omega_{emu}}{dt}\right) \quad \text{(C.5)}$$

After compensation, the system dynamics can be expressed in transfer function form, leading to Eqs. (5) and (6) presented in the main text.

Appendix D. 4S-VSI Voltage Modeling

Appendix D provides the detailed derivation of the 4S-VSI output voltage expressions and reference voltage relationships used in the modulation scheme.

The voltage across the DC-link capacitor can be separated into two components: a fluctuating voltage v_c and a direct voltage v_{c1} and v_{c2} as:

$$\begin{cases} v_c = -\dfrac{1}{2C}\int i_c(t)dt \\ v_{c1} = \dfrac{v_{DC}}{2} - v_c \\ v_{c2} = \dfrac{v_{DC}}{2} + v_c \end{cases} \quad \text{(D.1)}$$

In order to generate a balanced voltage by the four-switch inverter according to the standard control strategy, the reference voltages are written as:

$$\begin{cases} v_a^{ref} = \sqrt{3}v_m\cos(\theta_r - \dfrac{\pi}{6} - \varphi) \\ v_b^{ref} = \sqrt{3}v_m\cos(\theta_r - \dfrac{\pi}{2} - \varphi) \end{cases} \quad \text{(D.2)}$$

Where v_a^{ref} and v_b^{ref} are respectively the a and b leg reference voltage modulated via Pulse Width Modulation (PWM), θ_r is the electrical rotor position, while v_m and φ are respectively the reference voltage and phase. The relation between line-to-neutral voltages and reference voltages is computed as follows:

$$\begin{cases} u_{an} = \dfrac{1}{3}\left(2v_a^{ref} - v_b^{ref} - v_c\right) \\ u_{bn} = \dfrac{1}{3}\left(2v_b^{ref} - v_a^{ref} - v_c\right) \\ u_{cn} = \dfrac{1}{3}\left(-v_a^{ref} - v_b^{ref} + 2v_c\right) \end{cases} \quad \text{(D.3)}$$